Thermal transport properties of IrSbSe

Yu Liu (刘育)[1,*] A. M. Milinda Abeykoon,[2] Niraj Aryal,[1] David Graf,[3] Zhixiang Hu (胡之翔),[1,4]
Weiguo Yin (尹卫国)[1] and C. Petrovic[1,4]

[1]*Condensed Matter Physics and Materials Science Department, Brookhaven National Laboratory, Upton, New York 11973, USA*
[2]*National Synchrotron Light Source II, Brookhaven National Laboratory, Upton, New York 11973, USA*
[3]*National High Magnetic Field Laboratory, Florida State University, Tallahassee, Florida 32306-4005, USA*
[4]*Materials Science and Chemical Engineering Department, Stony Brook University, Stony Brook, New York 11790, USA*

We report a thermal transport study of IrSbSe, which crystallizes in a noncentrosymmetric cubic structure with the $P2_13$ space group and shows a narrow-gap semiconducting behavior. The large discrepancy between the activation energy for conductivity [$E_\rho = 128(2)$ meV] and for thermopower [$E_S = 17.7(9)$ meV] from 200 to 300 K indicates a polaronic transport mechanism. The electrical resistivity varies as $\exp(T_0/T)^{1/4}$ and thermopower varies as $T^{1/2}$ at low temperatures, indicating that it evolves into Mott variable-range hopping dominant conduction with decreasing temperature. IrSbSe shows a relatively low value of thermal conductivity (~ 1.65 W/K m) and thermopower of about 0.24 mV/K around 100 K, yet poor electrical conductivity. On the other hand, a high vacancy defect concentration on both Ir and Sb atomic sites of up to 15% suggests a high defect tolerance and points to the possibility of a future improvement of carrier density by chemical substitution or defect optimization.

I. INTRODUCTION

New transition-metal chalcogenides may enable transformative changes in thermoelectric energy creation and conversion [1–3]. Ternary CoSbS with Kondo-insulator-like intrinsic magnetic susceptibility features a high value of thermopower up to 2.5 mV/K at 40 K but also a relatively large value of thermal conductivity ~ 100 W/K m near the thermopower peak temperature [4]. This inhibits the thermoelectric figure of merit $ZT = (S^2/\rho\kappa)T$, where S is thermopower, ρ is electrical resistivity, κ is thermal conductivity, and T is temperature.

Electronic correlations are important in many transition-metal and rare-earth-based materials [5,6]. A theoretical study confirms that the colossal thermopower in CoSbS is due to carrier correlation and a large increase of effective mass [7]. In addition, it was suggested that the thermoelectric power factor in CoSbS may show a 10^7 times increase in magnetic field due to the high spin-orbit coupling (SOC) effect on thermopower [7]. The SOC causes a considerable enhancement of electrical conductivity, which is rather sensitive to the Co atomic moment and yet leaves the phonon dispersion and thermal conductivity unaffected.

Iridium-based materials with strong SOC host a variety of exotic quantum phases but also properties of interest for applications [8–11]. In IrBiSe, for example, bulk electronic bands are split by giant spin-orbit splitting about 0.3 eV and are fully spin polarized [12]. The electronic states in IrBiSe with

a three-dimensional (3D) chiral spin texture with negative and positive chiralities along the crystallographic [111] direction are of interest for spin sensor applications and could exhibit spin-triplet superconductivity upon doping [12].

In this paper, we report the thermal transport properties of noncentrosymmetric and cubic IrSbSe, isostructural to IrBiSe. We observed vacancy defects on both Ir and Sb atomic sites, i.e., $Ir_{0.90}Sb_{0.85}Se$ stoichiometry, leading to low values of thermal conductivity. The large discrepancy between the activation energy for electrical conductivity and for thermopower from 200 to 300 K suggests a polaronic transport mechanism. With decreasing temperature, it evolves into a Mott variable-range hopping dominant mechanism at low temperatures. Whereas high values of electrical resistivity inhibit ZT, a relatively high tolerance of the crystal structure to defect formation may allow for further carrier tuning and optimization of the thermoelectric performance, similar to IrBiSe [12].

II. EXPERIMENTAL DETAILS

An IrSbSe polycrystal was synthesized via a solid state reaction starting from an intimate mixture of high-purity elements, Ir powder (4*N*, Alfa Aesar) and Sb and Se pieces (5*N*, Alfa Aesar) with a stoichiometric ratio. The starting materials were mixed and ground in an agate mortar, pressed into a pellet, and sealed in an evacuated quartz tube backfilled with pure argon gas. The tube was heated to 500 °C and dwelled for 12 h, and then slowly heated to 800 °C and reacted for 5 days, followed by furnace cooling. The chemical composition was determined by multiple point energy-dispersive x-ray spectroscopy (EDS) in a JEOL LSM-6500 scanning electron microscopy (SEM). A synchrotron powder x-ray diffraction

———
*Present address: Los Alamos National Laboratory, Los Alamos, NM 87545, USA.

195116-1
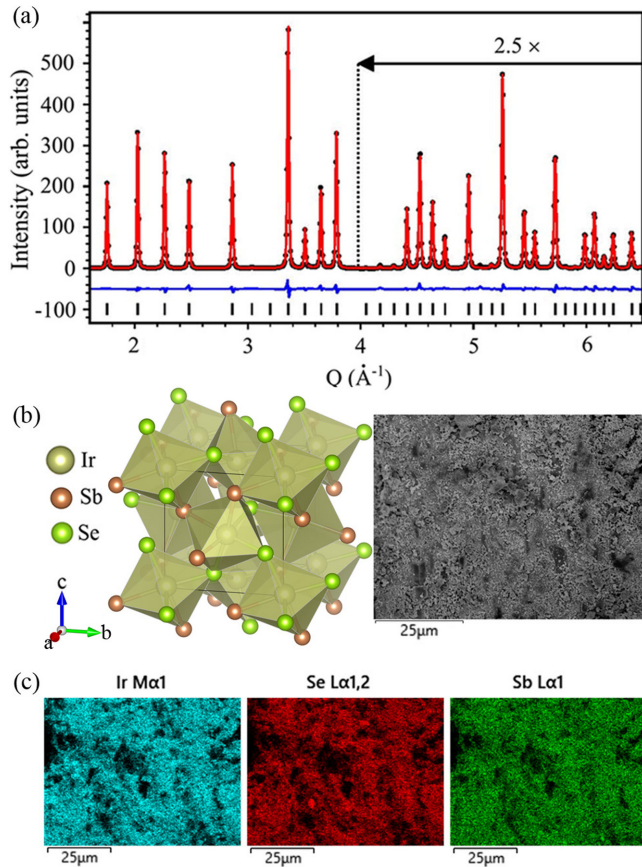
FIG. 1. (a) The Rietveld refinement of the background subtracted IrSbSe synchrotron powder x-ray diffraction. Plots show the observed (dots) and calculated (red solid line) powder patterns with a difference curve (blue). The black vertical tick marks represent Bragg reflections in the $P2_13$ space group. (b) Crystal structure and scanning electron microscopy (SEM) image along with (c) the energy dispersive spectroscopy (EDS) mapping on the IrSbSe sample.

(XRD) measurement was carried out in capillary transmission geometry using a Perkin Elmer amorphous silicon area detector at the 28-ID-1 pair distribution function (PDF) beamline of the National Synchrotron Light Source II (NSLS II) at Brookhaven National Laboratory (BNL). The setup utilized a ~74-keV ($\lambda = 0.166\,35$ Å) x-ray beam. Two-dimensional diffraction data were integrated using the FIT2D software package [13]. The Rietveld and PDF analyses were carried out using GSAS-II and PDFGUI software packages, respectively [14,15]. Electrical resistivity, thermopower, and thermal conductivity were measured in a Quantum Design physical property measurement system (PPMS-9) with the standard four-probe technique. Sample dimensions were measured by an optical microscope Nikon SMZ-800 with a resolution of 10 μm.

III. RESULTS AND DISCUSSIONS

Figure 1(a) shows the Rietveld refinement of synchrotron powder XRD for IrSbSe, indicating that all reflections can be well indexed in the $P2_13$ space group [16], and there are no extra impurity peaks. The determined lattice parameter

TABLE I. Atomic coordinates and displacements parameters for $Ir_{0.90(1)}Sb_{0.84(1)}Se$ obtained from Rietveld refinement at 300 K in a synchrotron powder XRD experiment.

Atom	Occupancy	x	y	z	U_{iso} (Å^2)
Ir	0.904(4)	0.0040(2)	0.0040	0.0040	0.0034
Sb	0.844(6)	0.3790(3)	0.3790	0.3790	0.0052(5)
Se	1.000	0.6235(4)	0.6235	0.6235	0.0010

$a = 6.204\,84(4)$ Å. The crystal structure is a derivative of the structure of iron pyrite (FeS$_2$) [16], which can also be viewed as a network of distorted IrSb$_3$Se$_3$ octahedra with each Sb or Se belonging to three such octahedra [Fig. 1(b)]. The EDS mapping presented in Fig. 1(c) shows that the ratio of Ir : Sb : Se $\approx 33(3) : 35(3) : 31(3)$, however, the Rietveld refinement indicates vacancy defects on both Ir and Sb atomic sites (Table I). The vacancy defect concentration is considerable, about 10% on Ir and 15% on Sb atomic sites, respectively.

Figure 2 shows the magnetic susceptibility of IrSbSe measured from 2 to 300 K in a magnetic field of $H = 10$ kOe, which shows no evidence of long-range magnetic ordering below 300 K, and follows the Curie-Weiss behavior. The inverse susceptibility was modeled by the Curie-Weiss law, $\chi(T) = \chi_0 + C/(T - \theta_W)$, where C is the Curie constant, θ_W is the Weiss temperature, and $\chi_0 = -8 \times 10^{-5}$ emu mol^{-1} Oe^{-1} is the temperature-independent diamagnetic term. The linear fit in the inset of Fig. 2 gives $\theta_W = -3$ K and $C = 1.67 \times 10^{-3}$ emu K mol^{-1} Oe^{-1}. The derived effective moment of $\mu_{eff} = \sqrt{8C} \approx 0.12\mu_B$/Ir is considerably smaller than the value of $2.83\mu_B$/Ir expected for spin-only $S = 1$ with Ir^{5+} ($5d^4$) ions. Similar magnetic behavior was also reported in Ir^{5+} compounds NaIrO$_3$ and KIrO$_3$ [17,18].

The temperature dependence of electrical resistivity $\rho(T)$ for IrSbSe is depicted in Fig. 3(a), showing an obvious semiconducting behavior. The value of $\rho_{300\,K}$ at room temperature is ~1.2 Ω m. It is plausible to consider three typical models to describe the semiconducting behavior: (i) a thermally
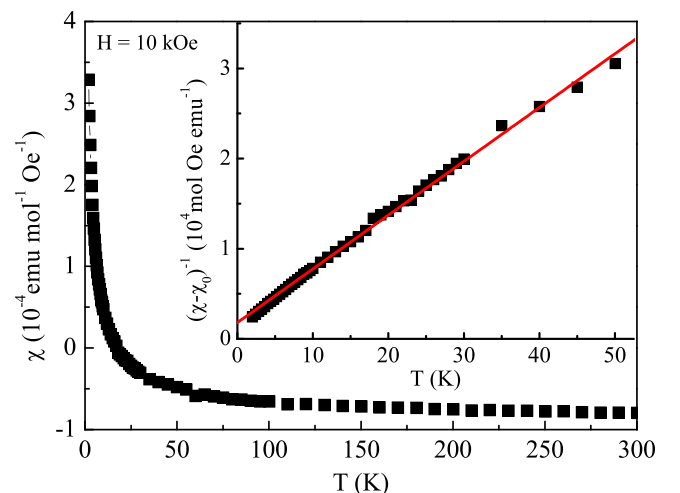
FIG. 2. Temperature dependence of magnetic susceptibility $\chi(T)$ for IrSbSe. The inset shows a Curie-Weiss plot with a fit to the Curie-Weiss law as explained in the main text.
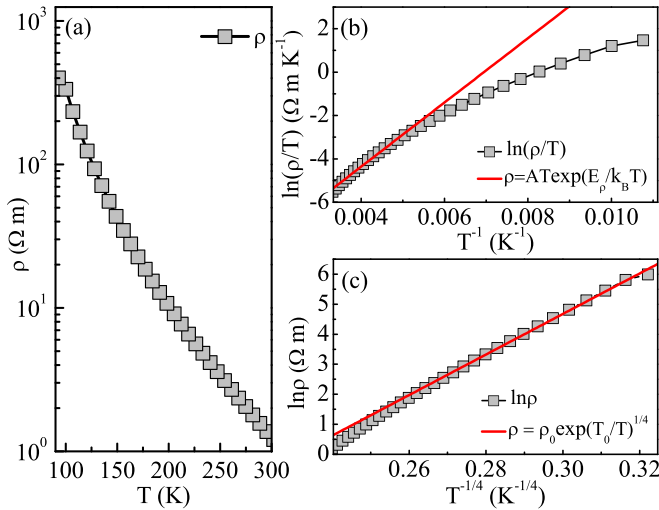
FIG. 3. (a) Temperature dependence of electrical resistivity $\rho(T)$ for IrSbSe. (b) $\ln(\rho/T)$ vs T^{-1} fitted by the adiabatic small polaron hopping model from 200 to 300 K. (c) $\ln\rho$ vs $T^{-1/4}$ fitted by the Mott variable-range hopping model from 100 to 200 K.

FIG. 4. (a) Temperature dependence of thermopower $S(T)$ for IrSbSe. (b) $S(T)$ vs T^{-1} fitted by using $S(T) = (k_B/e)(\alpha + E_S/k_B T)$ from 200 to 300 K. (c) $S(T)$ vs $T^{1/2}$ with a linear fit from 100 to 121 K.

activated model $\rho(T) = \rho_0 \exp(E_\rho/k_B T)$, where E_ρ is an activation energy; (ii) an adiabatic small polaron hopping model $\rho(T) = AT \exp(E_\rho/k_B T)$ [21–23]; and (iii) a Mott variable-range hopping (VRH) model $\rho(T) = \rho_0 \exp(T_0/T)^{1/4}$, where T_0 is a characteristic temperature and is related to the density of states available at the Fermi level $N(E_F)$ and carrier localization length. To understand the transport mechanism in IrSbSe, it is necessary to fit the $\rho(T)$ data based on these three formulas. Figure 3(b) shows the fit result of the adiabatic small polaron hopping model. The extracted activation energy E_ρ is $\sim$128(2) meV from 200 to 300 K, thus the band gap is estimated $\sim$256(4) meV. However, the $\rho(T)$ curve can also be well fitted using the thermally activated model (not shown here). With decreasing temperature, the $\rho(T)$ data from 100 to 200 K obey the Mott VRH model [Fig. 3(c)]. The derived characteristic temperature $T_0 \sim 2.1(1) \times 10^8$ K for Mott VRH conduction, and the corresponding localization length $\xi \sim 1.1$ Å given by $\xi^3 = 18/[k_B T_0 N(E_F)]$ [19,20], where $N(E_F)$ is the density of states at the Fermi level.

To distinguish the thermally activated model and polaron hopping model, we further measured temperature-dependent thermopower S [Fig. 4(a)]. The $S(T)$ shows negative values in the high-temperature regime with a relative large value of $\sim -101 \mu$V K^{-1} at 300 K, indicating dominant electronlike carriers. With decreasing temperature, $S(T)$ changes its slope and the sign from negative to positive below 130 K, suggesting the holelike carriers dominate at low temperatures. As shown in Fig. 4(b), the $S(T)$ vs T^{-1} curve can be well fitted with the equation $S(T) = (k_B/e)(\alpha + E_S/k_B T)$ [21], where E_S is an activation energy and α is a constant. The obtained activation energy for thermopower is $E_S = 17.7(9)$ meV from 200 to 300 K [Fig. 3(b)], which is much smaller than that for conductivity $E_\rho = 128(2)$ meV [Fig. 3(b)]. This large discrepancy between E_S and E_ρ typically reflects the polaron transport mechanism of carriers. Within the polaron hopping model, E_S is the energy required to activate the hopping of carriers, while E_ρ is the sum of energy needed for the creation of
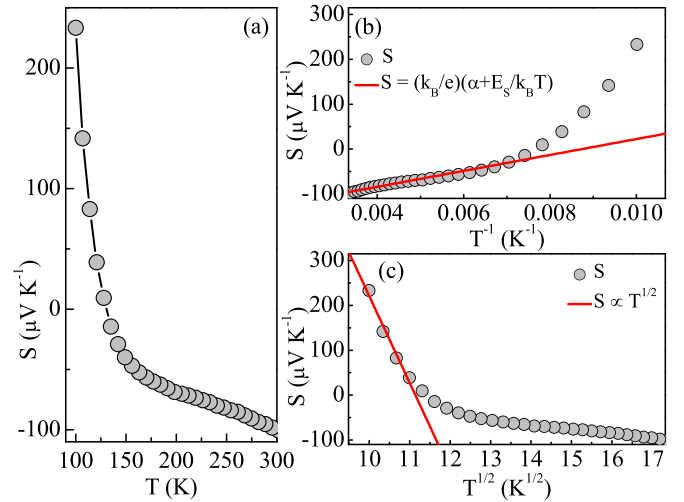
carriers and activating the hopping of carriers [21]; therefore, E_S is smaller than E_ρ. The weak temperature-dependent $S(T)$ at high temperatures also supports small polaron conduction. With decreasing temperature, the resistivity evolves into the Mott VRH dominant mechanism [Fig. 3(c)]. Within the Mott VRH model the $S(T)$ can be described by $S(T) = S_0 + AT^{1/2}$ [24]; it can be seen from the rapid slope change of $S(T)$, and S varies as $T^{1/2}$ from 100 to 121 K [Fig. 4(c)].

Figure 5(a) presents the temperature dependence of thermal conductivity $\kappa(T)$ for IrSbSe. Generally, $\kappa_{\text{total}} = \kappa_e + \kappa_L$, consisting of the electronic charge carrier part κ_e and the phonon term κ_L. The κ_e estimated from the Wiedemann-Franz law is negligibly small due to the large electrical resistivity of IrSbSe, indicating a predominantly phonon contribution. The $\kappa(T)$ shows a relatively low value of $\sim$1.85 W/K m at 200 K due to its structural complexity such as high nonstoi-
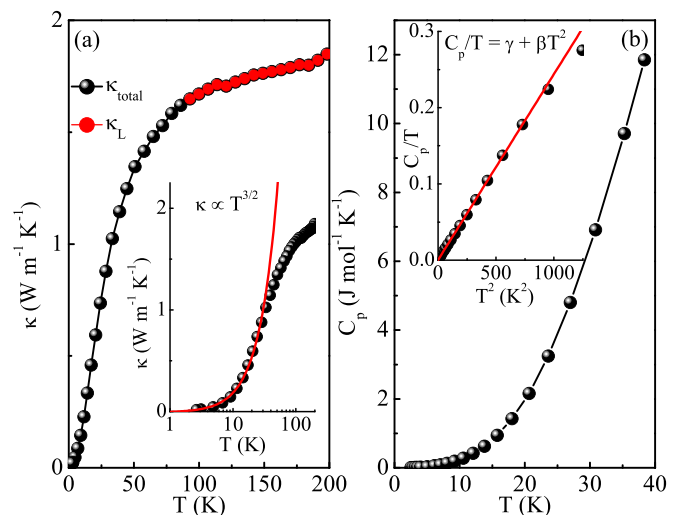
FIG. 5. Temperature dependence of (a) thermal conductivity $\kappa(T)$ and (b) heat capacity $C_p(T)$ for IrSbSe.

chiometry. With decreasing temperature, $\kappa(T)$ follows a $T^{3/2}$ dependence below 30 K [inset in Fig. 5(a)]. This deviates from the common $\kappa \sim T^3$ usually observed in bulk crystals or thin films [25,26], and it is close to the power law observed in the thermal conductivity of nanostructures due to grain size variation [27,28]. This might imply nanostructural differences that are induced by different vacancy defects, in particular grains and associated phonon frequency changes. It should be noted that IrSbSe shows a relatively low value of thermal conductivity ~ 1.65 W/K m and a thermopower of ~ 0.24 mV/K around 100 K, yet poor electrical conductivity, leading to rather small values of the power factor ($<10^{-2}$ μW/m K^2) and zT ($<10^{-6}$). The specific heat $C_p(T)$ of IrSbSe at low temperatures is depicted in Fig. 5(b). By fitting the C_p/T vs T^2 data below 30 K by using $C_p(T)/T = \gamma + \beta T^2$, we obtain the Sommerfeld electronic specific-heat coefficient $\gamma \sim 0.4(2)$ mJ mol^{-1} K^{-2}, as expected for an insulating ground state. The derived Debye temperature $\Theta_D = 288(1)$ K from $\beta = 0.244(1)$ mJ/mol K by using the equation $\Theta_D = [12\pi^4 NR/(5\beta)]^{\frac{1}{3}}$, which implies an average sound velocity of $\nu_s \approx 2600$ m/s [29]. The phonon mean free path $l_\kappa \sim 0.5$ μm at 2 K is estimated from the heat capacity and thermal conductivity via $\kappa_L = C_p \nu_s l_\kappa / 3$ [30].

We note that the polaronic transport is favored in materials with strong SOC that lack inversion symmetry [31]. To get insight into the relevance of SOC, we further performed first-principles calculations using density functional theory. We applied the WIEN2K [32] implementation of the full potential linearized augmented plane-wave method in the generalized gradient approximation using the Perdew-Burke-Ernzerhof (PBEsol) functional [33] on stoichiometric IrSbSe [16]. The SOC is treated in the second variation method. The basis size was determined by $R_{mt}K_{max} = 7$ and the Brillouin zone was sampled with a regular $15 \times 15 \times 15$ mesh containing 176 irreducible k points to achieve an energy convergence of 1 meV. As shown in Figs. 6(a)–6(d), the calculated band structure and atom-resolved density of states (DOS) indicates that the system is a nonmagnetic semiconductor. There is a band gap of about 1 eV for the calculations without SOC [Figs. 6(a) and 6(b)] and about 0.9 eV for the case with SOC [Figs. 6(c) and 6(d)]. The total DOS (black line) rises rapidly from the band edges with the band character being mainly of Ir 5d orbitals. However, the contributions from Sb and Se p orbitals are significant in reducing the Ir 5d orbital weight, compared with the dominant character of the transition metal in CoSbS and FeSbS [34]. This weakens magnetic instability, if any, upon charge doping. The effects of SOC are more clearly seen in the band structures [Figs. 6(a) and 6(b)], where the SOC inducing the band splitting is about 0.2 eV for the valence bands around the Fermi level. The band-structure plots also suggest that the valence and conduction bands are substantially massive. These are similar to the results for IrBiSe [12], where a SOC splitting of about 0.3 eV was reported. Thus, the split band in stoichiometric IrSbSe is also expected to be fully spin polarized with a 3D chiral spin texture [12]. The present off-stoichiometric polycrystalline sample with a much smaller band gap suggests the occurrence of in-gap states.

In order to compare with the experimental thermopower (S), we calculate S in the presence of SOC within the rigid band constant relaxation time approximation as implemented
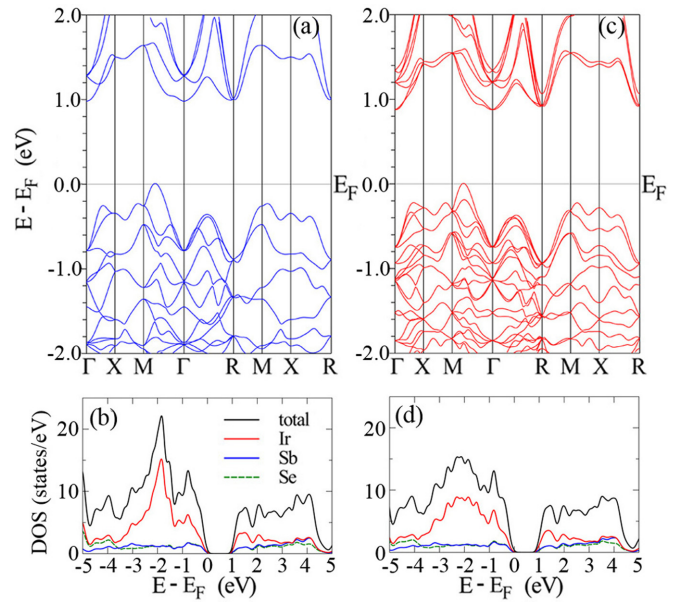
FIG. 6. (a) Band structure and (b) the atom-resolved density of states (DOS) calculated without spin-orbit coupling (SOC) on stoichiometric IrSbSe. (c) Band structure and (d) the DOS calculated with SOC.

in the BOLTZTRAP2 software package [35]. As shown in Fig. 7(a), the variation of S with electron carrier concentration (n) for different temperatures shows Pisarenko behavior, i.e., logarithmic in carrier concentration, for a wide range of temperature and n. Such behavior has also been observed in many other semiconductors including CoSbS which lies in the same family [34]. To make a more direct comparison with the experimental data, we also studied the temperature dependence of S for different values of n [Fig. 7(b)]. For this plot, we fix the value of n at $T = 300$ K and take into account the temperature dependence of $n(T) = \int_{E_c}^{\infty} dE g_c(E)/[e^{(E-\mu)/k_B T} +$
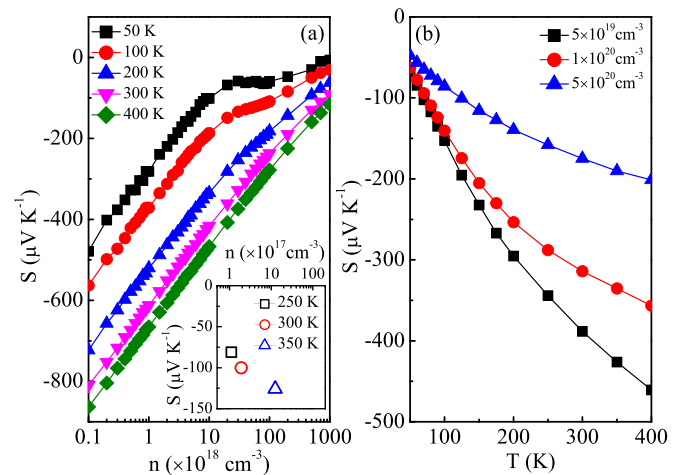
FIG. 7. Variation of calculated thermopower S for the electron-doped case (a) as a function of carrier concentration n for different temperatures and (b) as a function of temperature for different values of n. The inset in (a) shows the experimental S and n at the indicated temperatures.
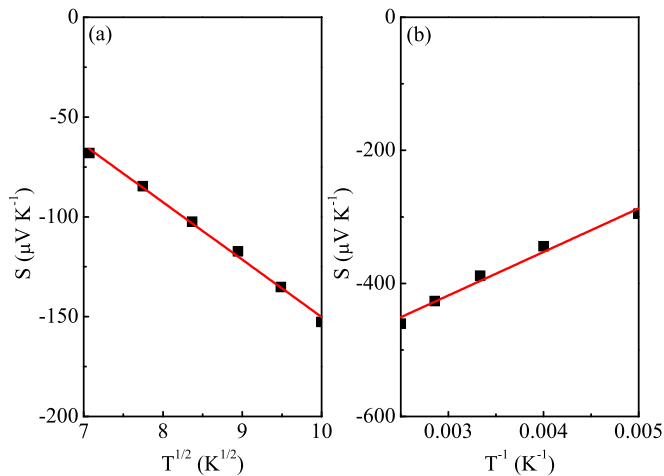
FIG. 8. Fitting of the calculated thermopower S with $n(300\,\text{K}) = 5 \times 10^{19}$ cm^{-3} in linear dependence of (a) $T^{1/2}$ and (b) T^{-1} at low and high temperatures, respectively, similar to the experimental observation.

1] [36], where g_c is the density of states of conduction bands, E_c is the conduction band edge, and μ is the chemical potential at that temperature. The temperature dependence of μ is obtained from the Sommerfeld relationship $\mu(T) = E_\text{F} - \pi^2 k_\text{B}^2 T^2 g'(E_\text{F})/6g(E_\text{F})$. The calculated magnitude of S decreases as temperature decreases, in agreement with the experiment.

The Hall coefficient measured in the present polycrystalline sample is negative at room temperature, in agreement with the negative value of $S(300\,\text{K})$ [Fig. 4(a)]. The derived carrier concentration $n(300\,\text{K}) \sim 1.9(1) \times 10^{17}$ cm^{-3}; it increases to $n(350\,\text{K}) \sim 1.25(2) \times 10^{18}$ cm^{-3} [inset in Fig. 7(a)]. For the values of n calculated larger than the experimental ones, we find the magnitude as well as the temperature dependence of S are similar to the experimental results. As shown in Fig. 8, our calculation can reproduce the linear dependence of S with $T^{1/2}$ at low temperatures for the Mott VRH dominant conduction, and T^{-1} at high temperatures, respectively. The derived activation energy $E_S^\text{cal} =$

65(5) meV, which is larger than the experimental value of $E_s = 17.7(9)$ meV but still much smaller than $E_\rho = 128(2)$ meV, confirming the polaronic nature at high temperatures. However, we should note that the experimentally observed p-n transition at $T \sim 130$ K has not been reproduced by the simulation, calling for further investigation of the thermoelectric properties in this system beyond the constant relaxation time approximation by including temperature as well as energy and the momentum-dependent electron-phonon scattering rate. It is also plausible that such a p-n transition is a consequence of impurities in this system due to a large off-stoichiometry since it is not reported in a similar CoSbS single-crystal system [4]. Further efforts on single-crystal growth will be helpful to clarify this, and carrier optimization is needed to obtain better thermoelectricity performance.

IV. CONCLUSIONS

In summary, we observed poor electrical and thermal conductivity in an IrSbSe polycrystal. The electronic transport mechanism indicates the polaronic nature at high temperatures and Mott VRH conduction at low temperatures. The thermopower is also simulated by using an *ab initio* calculation. Structurally, IrSbSe crystallizes in the $P2_13$ space group even with a high vacancy defect concentration, i.e., with $\text{Ir}_{0.90}\text{Sb}_{0.85}\text{Se}$ stoichiometry. Such a high defect tolerance implies possibilities for future carrier optimization by vacancy defects and chemical doping.

[1] S. Roychowdhury, M. Samanta, A. Banik, and K. Biswas, Thermoelectric energy conversion and topological materials based on heavy metal chalcogenides, J. Solid State Chem. **275**, 103 (2019).

[2] Y. Ouyang, Z. Zhang, D. Li, J. Chen, and G. Zhang, Emerging theory, materials, and screening methods: New opportunities for promoting thermoelectric performance, Ann. Phys. **531**, 1800437 (2019).

[3] A. Banik, S. Roychowdhury, and K. Biswas, The journey of tin chalcogenides towards high-performance thermoelectrics and topological materials, Chem. Commun. **54**, 6573 (2018).

[4] Q. Du, M. Abeykoon, Y. Liu, G. Kotliar, and C. Petrovic, Low-Temperature Thermopower in CoSbS, Phys. Rev. Lett. **123**, 076602 (2019).

[5] G. Palsson and G. Kotliar, Thermoelectric Response Near the Density Driven Mott Transition, Phys. Rev. Lett. **80**, 4775 (1998).

[6] W. Koshibae and S. Maekawa, Effects of Spin and Orbital Degeneracy on the Thermopower of Strongly Correlated Systems, Phys. Rev. Lett. **87**, 236603 (2001).

[7] R. Gupta and C. Bera, Spin-orbit coupling effect on the thermopower and power factor of CoSbS, Phys. Rev. B **101**, 155206 (2020).

[8] J. G. Rau, E. K.-H. Lee, and H.-Y. Kee, Spin-orbit physics giving rise to novel phases in correlated systems: Iridates related materials, Annu. Rev. Condens. Matter Phys. **7**, 195 (2016).

[9] H. Takagi, T. Takayama, G. Jackeli, G. Khaliullin, and S. E. Nagler, Concept and realization of Kitaev quantum spin liquids, Nat. Rev. Phys. **1**, 264 (2019).

[10] X. Wan, A. M. Turner, A. Vishwanath, and S. Savrasov, Topological semimetal and Fermi-arc surface states in the electronic structure and pyrochlore iridates, Phys. Rev. B **83**, 205101 (2011).

[11] Y. Liu, H. Lei, K. Wang, M. Abeykoon, J. B. Warren, E. Bozin, and C. Petrovic, Thermoelectric studies of $Ir_{1-x}Rh_xTe_2$ ($0 \leqslant x \leqslant 0.3$), Phys. Rev. B **98**, 094519 (2018).

[12] Z. Liu, S. Thirupathaiah, A. N. Yaresko, S. Kushwaha, Q. Gibson, W. Xia, Y. Guo, D. Shen, R. J. Cava, and S. V. Borisenko, A giant bulk-type Dresselhaus splitting with 3D chiral spin texture in IrBiSe, Phys. Status Solidi RRL **14**, 1900684 (2020).

[13] A. P. Hammersley, S. O. Svenson, M. Hanfland, and D. Hauserman, Two-dimensional detector software: From real detector to idealised image or two-theta scan, High Press. Res. **14**, 235 (1996).

[14] B. H. Toby, EXPGUI, a graphical user interface for GSAS, J. Appl. Crystallogr. **34**, 210 (2001).

[15] C. L. Farrow, P. Juhas, J. W. Liu, D. Bryndin, E. S. Bozin, J. Bloch, T. Proffen, and S. J. L. Billinge, PDFfit2 to PDFgui: Computer programs for studying nanostructure in crystals, J. Phys.: Condens. Matter **19**, 335219 (2007).

[16] F. Hulliger, New compounds with cobaltite structure, Nature (London) **198**, 382 (1963).

[17] D. C. Wallace and T. M. McQueen, New honeycomb Iridium(V) oxides: $NaIrO_3$ and $Sr_3CaIr_2O_9$, Dalton Trans. **44**, 20344 (2015).

[18] S. Guo, K. M. Powderly, and R. J. Cava, Synthesis, structure, and magnetism of BCC $KIrO_3$, Dalton Trans. **49**, 12018 (2020).

[19] R. Hu, V. F. Mitrovic, and C. Petrovic, Anisotropy in the magnetic and electrical transport properties of $Fe_{1-x}Cr_xSb_2$, Phys. Rev. B **76**, 115105 (2007).

[20] J. R. Friedman, Y. Zhang, P. Dai, and M. P. Sarachik, Magnetic-field-induced crossover from Mott variable-range hopping to weakly insulating behavior, Phys. Rev. B **53**, 9528 (1996).

[21] I. G. Austin and N. F. Mott, Polarons in crystalline and non-crystalline materials, Adv. Phys. **50**, 757 (2001).

[22] Y. Liu, C.-J. Kang, E. Stavitski, Q. Du, K. Attenkofer, G. Kotliar, and C. Petrovic, Polaronic transport and thermoelectricity in $Fe_{1-x}Co_xSb_2S_4$ ($x = 0$, 0.1, and 0.2), Phys. Rev. B **97**, 155202 (2018).

[23] Y. Liu, Z. Hu, M. Abeykoon, E. Stavitski, K. Attenkofer, E. D. Bauer, and C. Petrovic, Polaronic transport and thermoelectricity in $Mn_3Si_2Te_6$ single crystals, Phys. Rev. B **103**, 245122 (2021).

[24] I. P. Zvyagin, On the theory of hopping transport in disordered semiconductors, Phys. Status Solidi B **58**, 443 (1973).

[25] *Thermophysical Properties of Matter*, edited by Y. S. Touloukian (IFI/Plenum, New York, 1970–1979).

[26] A. D. McConnell and K. E. Goodson, Thermal conduction in silicon micro- and nanostructures, Annu. Rev. Heat Transfer **14**, 129 (2005).

[27] Z. Wang, J. E. Alaniz, W. Jang, J. E. Garay, and C. Dames, Thermal conductivity of nanocrystalline silicon: Importance of grain size and frequency-dependent mean free paths, Nano Lett. **11**, 2206 (2011).

[28] H. Zhao, M. Pokharel, G. Zhu, S. Chen, K. Lukas, Q. Jie, C. Opeil, G. Chen, and Z. Ren, Dramatic thermal conductivity reduction by nanostructures for large increase in thermoelectric figure-of-merit of $FeSb_2$, Appl. Phys. Lett. **99**, 163101 (2011).

[29] Orson L. Anderson, A simplified method for calculating the Debye temperature from elastic constants, J. Phys. Chem. Solids **24**, 909 (1963).

[30] Q. Du, X. Tong, Y. Liu, and C. Petrovic, Suppression of thermal conductivity and electronic correlations in $Fe_{1-x}Ru_xSb_2$ ($0 \leqslant x \leqslant 0.6$), Appl. Phys. Lett. **118**, 171904 (2021).

[31] C. Grimaldi, Large polaron formation induced by Rashba spin-orbit coupling, Phys. Rev. B **81**, 075306 (2010).

[32] K. Schwarz, P. Blaha, and G. K. H. Madsen, Electronic structure calculations of solids using the WIEN2k package for material sciences, Comput. Phys. Commun. **147**, 71 (2002).

[33] J. P. Perdew, A. Ruzsinszky, G. I. Csonka, O. A. Vydrov, G. E. Scuseria, L. A. Constantin, X. Zhou, and K. Burke, Restoring the Density-Gradient Expansion for Exchange in Solids and Surfaces, Phys. Rev. Lett. **100**, 136406 (2008).

[34] D. Parker, A. F. May, H. Wang, M. A. McGuire, B. C. Sales, and D. J. Singh, Electronic and thermoelectric properties of CoSbS and FeSbS, Phys. Rev. B **87**, 045205 (2013).

[35] G. K. H. Madsen, J. Carrete, and M. J. Verstraete, BoltzTraP2, a program for interpolating band structures and calculating semiclassical transport coefficients, Comput. Phys. Commun. **231**, 140 (2018).

[36] N. W. Ashcroft and N. D. Mermin, *Solid State Physics* (Cengage Learning, Boston, 2011).